Journal of Power Sources 201 (2012) 307–321

Contents lists available at SciVerse ScienceDirect

Journal of Power Sources

journal homepage: www.elsevier.com/locate/jpowsour

Calibration and finite element simulation of pouch lithium-ion batteries for mechanical integrity

Elham Sahraei [1], Rich Hill, Tomasz Wierzbicki *

Impact and Crashworthiness Lab, Massachusetts Institute of Technology, 77 Massachusetts Ave, Room 5-218, Cambridge, MA 02139, United States

ARTICLE INFO

Article history:
Received 4 August 2011
Received in revised form 23 October 2011
Accepted 24 October 2011
Available online 3 November 2011

Keywords:
Pouch cell
Lithium-ion battery
Constitutive modeling
FE simulation
Short circuit

ABSTRACT

Mechanical tests were performed on pouched and bare lithium-ion cells under five loading conditions. These included through-thickness compression, in-plane unconfined compression, in-plane confined compression, hemispherical punch indentation and three-point bending. From the measured load–displacement data, the individual compression stress–strain curves were calculated for the separator, the active anode and cathode materials. The FE model was developed, composed of shell elements, representing the Al and Cu foil, and solid elements for the active material with a binder lumped together with the separator. Very good correlation was obtained between LS Dyna numerical simulation and test results for the through-thickness compression, punch indentation and confined compression. Closed form solutions were also derived to reveal the underlying physics and identify important groups of parameters. It was also demonstrated that a thin pouch enclosure provided considerable reinforcement and in some cases changed the deformation and failure mechanism. The present computational model of an individual cell provides a fundamental building block for modeling battery modules and battery packs across different length scales. The present test program differs substantially from the nail indentation or punch crush loading performed by the industry, and provides data for the development of an advanced constitutive model needed for strength/weight optimization and safety assessments of Li-ion batteries.

1. Introduction

There are three interrelated aspects of battery design: electrochemistry, thermal management, and mechanical integrity. The electromechanical process begins at the level of the electrode/separator assembly and most of the advances and closely guarded secrets of the energy storage capacity are in the composition of the active electrode material. Independent of exact chemistry, all lithium-ion batteries are built in the same way: as a layered structure consisting of a negative electrode (commonly referred to as the anode), a positive electrode (commonly referred to as a cathode), a polyolefin separator, and current collectors for both electrodes. While thicker coatings enable higher energy storage, thinner coatings enable higher power capability. In addition to the multi-physics problem, the challenge in battery modeling is that it involves six orders of magnitude levels in length, see Fig. 1. The present paper is covering only two size levels, encircled in Fig. 1.

It is not the purpose of this paper to review the enormous progress of research on electrochemistry. General information on trends and developments in the battery industry can be found in the proceedings of the International AABC and EVS conference series. When studying recent papers published in the Journal of Power Sources and other leading journals, it is evident that most of the articles report on advances on electrochemistry. The existing papers on mechanical modeling of the cell are actually restricted to the level of electrode/separator assembly. For example, the effect of the process of intercalation on stress/strains in the particle or separator level was studied among others by [1–9]. Interesting "pinching" tests with punch radii 9.5–25 mm were recently reported in [10]. In these tests measured was the voltage and surface temperature as a function of the punch stroke in order to predict failure of the separator and the onset of electric short circuit. No information of the force level was provided in that paper.

There is a general understanding that the current lithium polymer batteries are constructed as very weak composites consisting of layers of foils and separator sandwiched between graphite and metal oxide particles and held together by a binder. There is no adhesive between layers of electrode/separator assembly. The tensile and compressive forces of the electrode/separator assembly are then controlled to a large extent by the strength of the binder. Liu et al. presented a concept of reinforcing the active

* Corresponding author. Tel.: +1 617 253 2104; fax: +1 617 253 8689.
E-mail addresses: elhams@mit.edu (E. Sahraei), richhill@mit.edu (R. Hill), wierz@mit.edu (T. Wierzbicki).
[1] Tel.: +1 617 324 5025.

0378-7753/$ – see front matter © 2011 Elsevier B.V. All rights reserved.
doi:10.1016/j.jpowsour.2011.10.094

Nomenclature

b	width
h_f	average thickness of foil
l	length
n	number of half waves
r_1	constant normalizing coefficient
t	thickness
w	downward displacement
A	power law coefficient
E	modulus of elasticity
H	thickness of cell
K	elastic stiffness
N	total number of foils
N_W	bucklingload per unit width
P_b	bucklingload of bare cell
P_P	bucklingload of pouched cell
P_{powder}	resistance force from powder
P_{foil}	resistance force from foil
R	radius of punch
δ	punch displacement
ε	strain
ε_v	volumetric strain
ε_{zz}	Strain in z direction
$\Delta\sigma_{foil}$	Buckling stress of foil
Δu	length difference
σ	stress
σ_0	average flow stress of foil
σ_{rz}	shear stress
σ_{zz}	stress in z direction
μ	coefficient of friction

electrode material by carbon fibers and then replacing the liquid electrolyte with solid-state polymer electrolyte [11]. They have demonstrated that the above modifications increase the tensile strength of the cathode by almost an order of magnitude. Likewise, the compressive strength of the electrode should also increase by a similar ratio. Despite advances at the micro level, it is difficult to find in the open literature any reports on computational models valid for plastic deformation and failure of the cell components, and capable of evaluating mechanical integrity of the cell in different abuse conditions. The approach undertaken here is a first step to provide insight for safety design and optimization of the cell under various mechanical loading conditions.

In this paper a computational model of pouch batteries is developed. The pouch batteries can be considered as multi-layered anisotropic thick plates. Lithium-ion batteries are made by winding, stacking or folding of a long ribbon of separator with intermittent active material on the two sides. A common feature of pouch batteries is that the electrode/separator assembly is stacked or folded instead of wound. Equally important is that the typical length dimension is much larger than the thickness. For example, commercially available pouch batteries are about 5–7 mm thick. The actual dimensions are not important; it is the length-to-thickness ratio that matters. The pouch batteries are sealed inside a flexible thin plastic/aluminum cover, while the prismatic batteries are housed inside a more-rigid plastic or metal container. Because of large unsupported area, the cladding offers considerable resistance in some loading directions and very little in others. The pouch "form factor" is prone to delamination and buckling. The buckling strength of the cell compressed in the width and length direction is relatively low due to the lack of shear and/or tension forces transmitted between individual layers.

There are number of mechanical and geometrical parameters that characterize the deformation process: the two new parameters identified in the present paper are the length scale and amount of lateral through-thickness constraints. In this pilot study an insight into mechanical performance is gained by physical testing, and numerical simulation. The present mechanical model of prismatic batteries and a similar model for cylindrical cells [12] are indispensible tools for the weight-efficient and safe design of batteries. Such models appear to be currently lacking in the open literature.

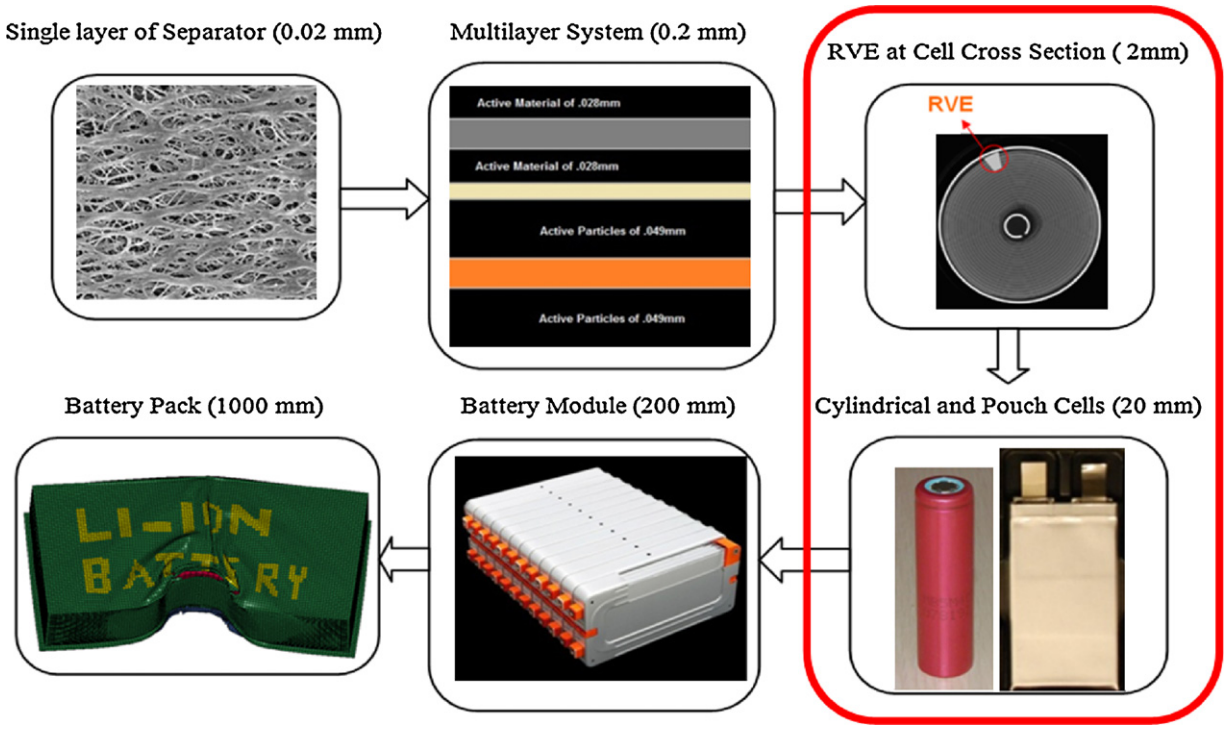

Fig. 1. Six orders of magnitudes in the length scale of lithium-ion batteries, the length scale addressed in this paper is encircled in red.

Table 1
Specifications of the lithium polymer pouch cells used for testing.

	Small pouch cell	Medium pouch cell
Nominal capacity	740 mAh	3.2 Ah
Nominal voltage	3.7 V	3.7 V
Thickness	5.35 mm	8.2 mm
Width	34 mm	43.5 mm
Length	59.5 mm	129.5 mm
Weight	19 g	85 g
Pouch thickness	0.14	0.11

2. Choice of batteries

The mechanical properties of lithium-ion batteries subjected to various types of loading depend on the "form factor". This form factor is determined by the particular arrangement of the electrode/separator assembly which may be wound, forming a cylindrical shape, or stacked, creating a prismatic shape. This paper is concerned with the pouch batteries.

Typical laboratory tests require cutting relatively small specimens from larger blocks in order to fit standard fixtures and to avoid exceeding the limits of testing equipment. Instead of cutting specimens from larger prismatic batteries, which by itself poses a formidable problem, it was decided to work on small pouch batteries, which already possess the ideal dimensions for laboratory tests. Unlike prismatic or cylindrical cells which contain a sheet-metal casing, pouch cells utilize a very thin covering which allows a more flexible cell. For the purpose of the present study that is aimed at developing general testing and modeling procedures, the choice of a particular manufacturer is unimportant. Commercially available lithium–polymer pouch batteries with lithium cobalt dioxide chemistry were purchased. The specifications of the pouch batteries, which were used for this study, are detailed in Table 1 and Fig. 2.

Both batteries were wrapped tightly by a soft casing made of aluminum plastic laminates, with a relatively low elastic modulus of 3–4 GPa but a tensile strength of approximately 180 MPa. Under some loading directions, these casings contributed significantly to the strength of the entire cell. All the tests were perfumed on pouched cells as received and then repeated on bare cells (by removing the pouch), therefore the contribution of pouch to the overall strength in all directions is fully documented. When the role of casing in structural integrity of the cell becomes clear, it can help manufacturers in design or selection of pouch material for future cells. Fully or partially discharged cells were tested in the MIT Impact and Crashworthiness Lab to minimize environmental impact. Hazardous controls further consisted of tightly controlling any spilled electrolyte. Tests are being planned together with the EMI Fraunhofer Institute in Freiburg, Germany on fully charged batteries [13].

3. Description of experiments and details of results

Seventeen batteries were tested under compressive load in five different load applications.

1. Compression between two plates.
2. Lateral indentation of the cell by a hemispherical punch.
3. Unconfined axial crush of the cell in the length and width direction.
4. Confined compression test of the cell in the width direction.
5. Three-point bending test of a medium-sized cell.

In all cases, the output of the experiments consisted of the measured load–displacement curve and photographs of the sequenced deformation. The Digital Image Correlation (DIC) available in the lab was not utilized in this preliminary round of tests. In future experiments the DIC will be particularly valuable in determining local displacement and strains. All tests were performed on an MTS load frame with either 10 kN or 200 kN load cells depending on the specimen size and the loading direction. The crosshead speed was chosen to vary between 0.5 and 3 mm min^{-1}. Testing of batteries under higher strain rates is the subject of future research.

In order to learn about the interior design of the cell and to measure thickness of individual components, the small pouch battery was disassembled. Information on thickness of individual components of the multi-layer system was not provided by the manufacturer, and therefore the measurements were performed in the lab. It was found that the interior of the "jelly-roll" was composed of two separate parts, each wrapped around by two windings of separator. This would suggest a global model of a laminate plate with two layers, $n = 2$. When unwinding each part, there were alternating anode and cathode coatings on the two sides of a ribbon-like separator, progressively folded rather than stacked, see Fig. 3. This type of design bears important implications on the strength of the cell as will be shown in Section 3.3.

The coated anodes and cathodes were easily disconnected from the polymeric separator, similar to a stack of cards. The active particle with binder was firmly adhered to the metallic foils. Altogether, there were 20 individualized copper anode plates, 18 double-sided coated aluminum plates, and four single sided coated aluminum plates, all separated by over 46 cell-sized layers of continuous separator. The thickness of the individual copper and aluminum plates was measured by washing away the active coating using a solvent. The thickness of the coated current collectors was measured both individually and as a stack and by dividing the stack height by the number of plates. Both methods gave near identical results. All data gathered is presented in Table 2 and further illustrated in Fig. 3.

3.1. Compression of the pouched cell between two plates

Two batteries, one bare cell and one cell contained in the original pouch, were subjected to large lateral compression of up to

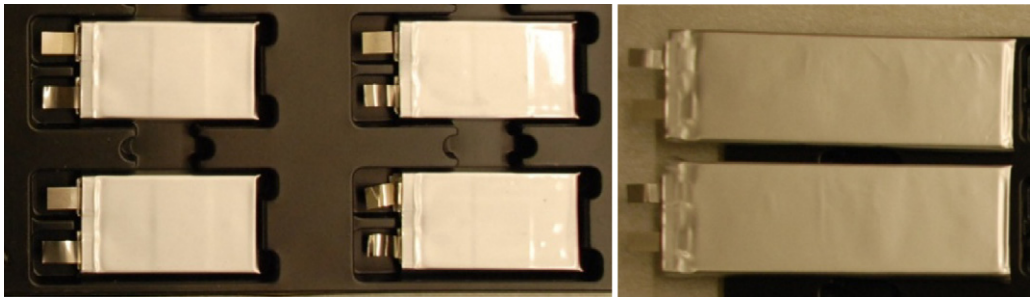

Fig. 2. Small and medium lithium–polymer pouch batteries.

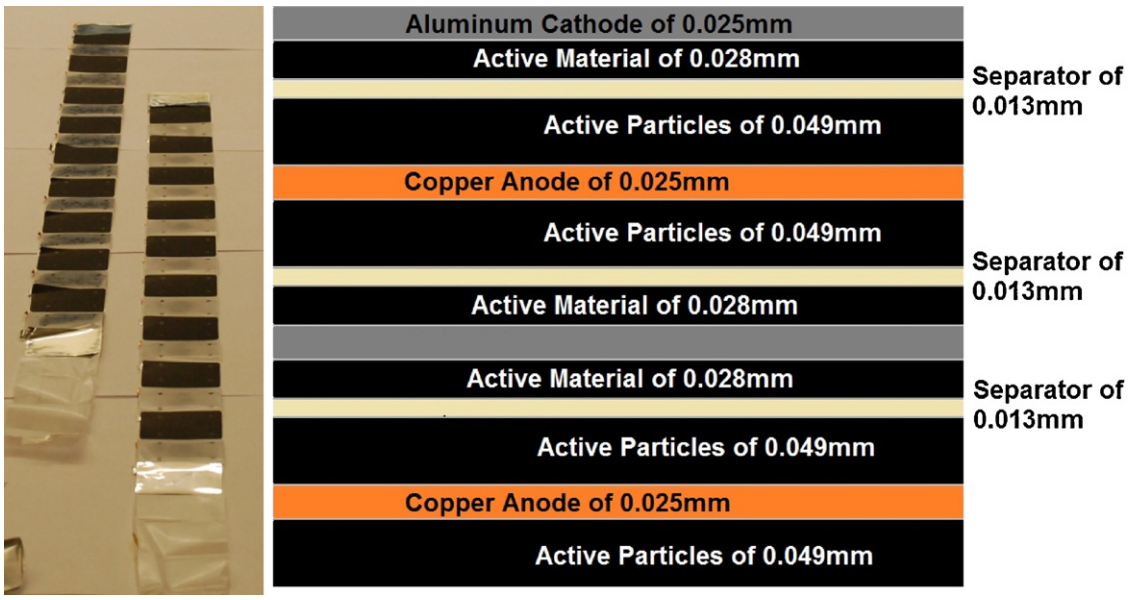

Fig. 3. Disassembled pouch cell into individual components (left) and a cross-section view (right).

Table 2
Direct measurements obtained of small lithium polymer cell contents.

All measurements in mm	Length	Width	Thickness, measured directly	Thickness, measured indirectly
Cu anode double-coated	50	30	0.117	0.116
Al cathode single coated	50	30	0.056	0.055
Al cathode double-coated	50	30	0.080	0.079
Separator	51.8	32	0.013	0.021
Copper foil	50	30	0.025	–
Aluminum foil	50	30	0.025	–

approximately one-half of the thickness. The recorded load displacement relationships are shown in Fig. 4.

At this crush distance, the force level is near the load-limit of the 200 kN MTS testing machine. In both cases, the electrolyte was squeezed from the cells which allowed for a volumetric change. The porosity of the active particles could be as high as 60% with the voids typically filled with electrolyte. Even though precise measurements were not taken, no visible increase in the lateral dimension of the specimen was observed. This suggests a very low Poisson ratio of the cell material for which a model of compressible foam could be used in the first approximation. In other words an almost uniaxial strain state was created in the tests. It is seen that the casing contributes very little in this lateral compressive direction. From the raw data on a bare cell shown in Fig. 4, the relationship between the average stress and volumetric strain was extracted, where the volumetric strain uses an engineering measurement (Fig. 19).

The measured relation between the stress and the average engineering strain provides the basis for subsequent numerical simulation. In addition to the average through-thickness properties, the strength of individual components was measured by performing compression tests of the stacks of identical current collectors (one stack each of aluminum and copper) and separator. The measured load–displacement curves were converted into stress–strain of the individual components, shown in Fig. 5. The compressive properties of coated Al and Cu electrodes are almost

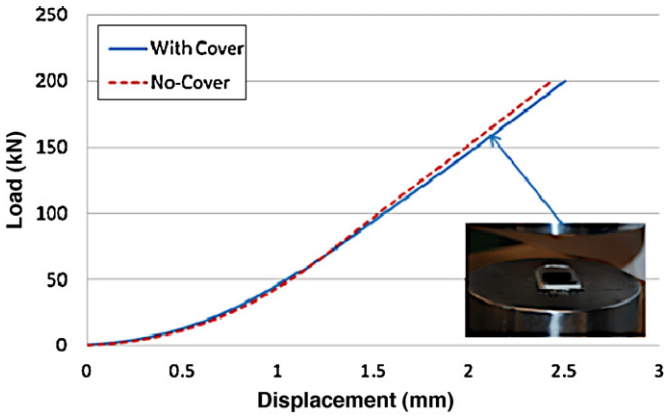

Fig. 4. Measured load–displacement of lateral compression of a bare and pouch cell.

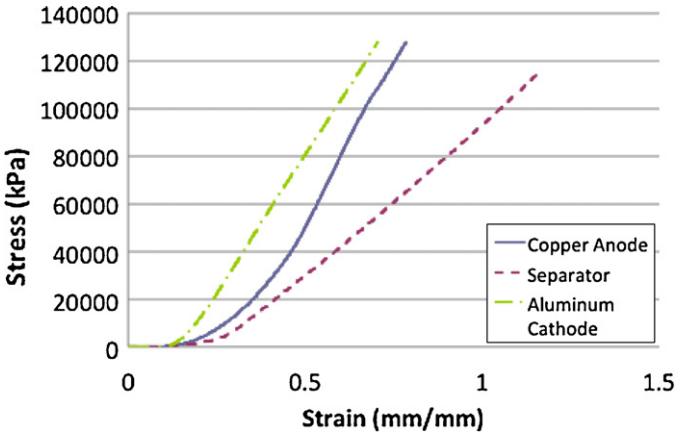

Fig. 5. Engineering stress strain for the load–displacement curve of cathode, separator, and anode.

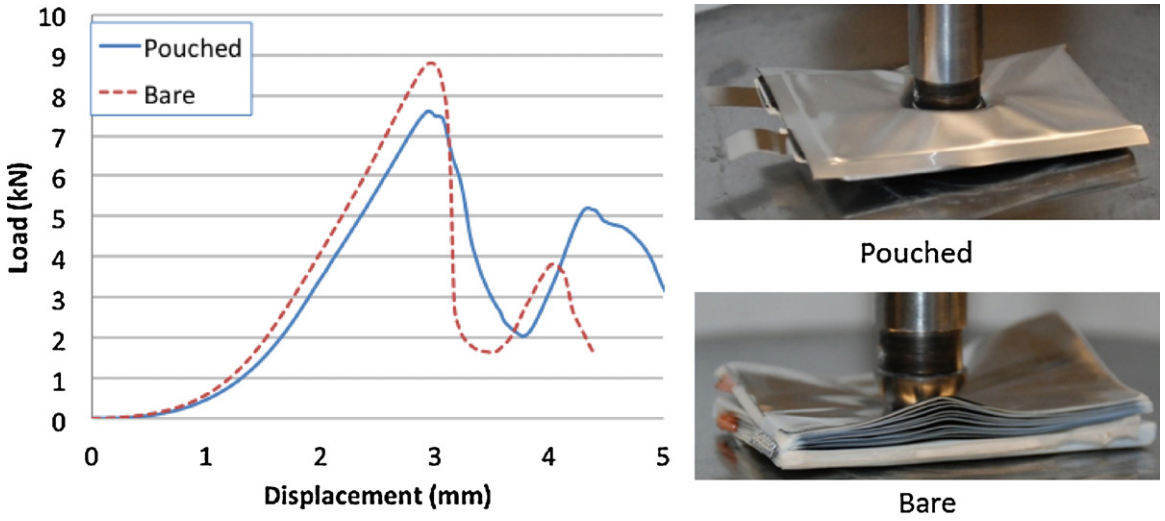

Fig. 6. Measured load–displacement curve for hemispherical punch indentation (left) with photographs of damaged cells (right).

the same and is similar to compressive properties of the separator. The generated data will be used in the future to develop the constitutive model of the Representative Volume Element (RVE) through the averaging procedure across a system of the electrode/separator. The accuracy of the present measuring technique does not allow the precise determination of the initial elastic modulus, which is important in simulation of the buckling problem.

3.2. Lateral Indentation of the cell by a hemispherical punch

The punch indentation test is relatively simple, does not produce exceedingly large forces and provides a wealth of information relevant to the task of modeling the layered structure of batteries. There is an axi-symmetric stress state under the punch, where through-thickness compressive stresses σ_{zz} and shear stress σ_{rz} are dominant in the active crushable material. The thin layer of foil is subjected to predominantly tensile stresses σ_{rr} under the punch and compressive stresses outside, leading to buckling. For this experiment, the radius of the hemispherical punch was chosen to be $R = 6.35$ mm, which is comparable to the thickness of the cell. It is thought that such geometry represents a realistic scenario of a foreign-object intrusion into a battery. This test is qualitatively different from the now-standard industry test of driving a nail into the cell, for example [14–16]. The measured load–displacement relation for bare and pouched cell is shown in Fig. 6.

There was little difference between the force level of pouched and bare cells. Bare batteries allowed observation of the interior over the experiment. During the test, a progressive fracturing and delamination of subsequent layers was observed. At the punch travel of approximately 3 mm, the load dropped indicating internal failure. Upon inspection there was a clear hole punched through a sizeable portion of the thickness of the cell. The indentation test of the bare cell produced a progressive delamination, circumferential buckling, and rising of the individual layers. The test of the cell confined by the pouch did not exhibit this phenomenon. The results of the punch indentation test were used for validation of the constitutive model developed during the lateral compression test, see Section 4.2. In the first set of punch tests, which were performed on the fully discharged cells, it was difficult to detect the actual onset of first rupture of the separator which would have caused an electrical short-circuit and possible thermal events. Therefore, this test was repeated with a partially discharged cell, to detect the exact onset of short circuit by measuring the voltage of the cell during the test. This was the only test on a partially charged cell. The state of charge was $50 \pm 10\%$. The voltage was monitored with a RadioShackDigital Multimeter. The initial voltage was 3.82 V. The onset of short circuit was determined from the drop in voltage. The load, displacement and voltage were recorded over time, and depicted in Fig. 7. This test produced very similar results to the first round of tests in terms of load–displacement data. This means the partial charge did not change the properties of the cells, and implicitly means that previous results on fully discharged cells are reliable to predict behavior of charged cells as well. A significant finding of this test was the fact that the point of short circuit detected from the drop in voltage was the exact same point that the load also dropped. The maximum load was 7.9 kN, which dropped to 5.4 kN within a second and to 2.47 in the next 2 s. At the same time, the original constant voltage of 3.82 V dropped to 0.125 V. The displacement at the point of maximum load was 2.9 mm. The sudden significant drop in force means that failure of one component in the multi-layer system immediately increased the force to other components over their limit and the cascading effect resulted in a simultaneous failure of several of components. It is planned to make symmetric through thickness cuts along the axes of the punch to see the details of the damage to interior layers.

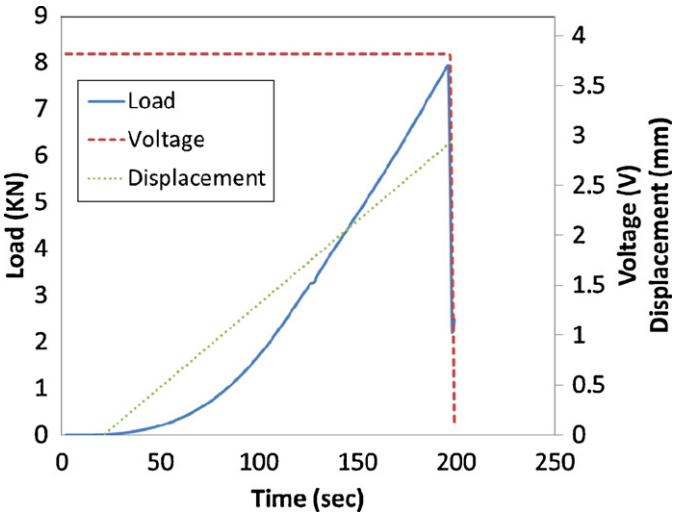

Fig. 7. Load displacement, and voltage from for hemispherical punch indentation test on a partially charged cell.

3.3. Analytical verification of test results

Further insight into the resistance of the cell to localized punch loading is obtained from the approximate closed-form solution of this problem. The present approach is valid for any given stress–strain relation of the compressible active powder. For simplicity, a parabolic fit is used, $\sigma_{zz} = A\varepsilon_v^2$, to describe the uniaxial stress–strain relationship of the active material with binder. It was calculated from Fig. 19 that the parameter $A = 566$ MPa. Aluminum and copper foils exhibit little hardening and can be modeled as rigid perfectly plastic material with the average flow stress σ_0. The fully calibrated multi-axial response of the active material with binder is currently lacking. Therefore, the approximate solution will be derived in this paper by considering only the axial (through-thickness) stress σ_{zz} and neglecting shear stress σ_{rz}. In the case of a uni-axial strain, the volumetric strain is simply the strain component in the z direction, defined by:

$$\varepsilon_v = \varepsilon_{zz} = \frac{w}{H} \tag{1}$$

where w is the downward displacement of a given material point under the punch, and H is the thickness of the cell. The vertical displacement of the material points under the punch $w(r,z)$ in the cylindrical coordinate system (r,θ,z) is approximated by the following function:

$$w(r,\theta) = \delta\left[1 - \left(\frac{r}{r_1}\right)^2\right] \tag{2}$$

where δ is the rigid punch displacement and r_1 is the outer radius of the contact area between the punch and the cell. For small indentation depths, $r_1 = \sqrt{2\delta R}$, where R is the radius of the hemispherical punch. It is further assumed that the trajectory of all material points are vertical such that the radial components of the displacement field as well as the hoop strain vanishes. The above displacement field satisfies all kinematic boundary conditions. Engineering strains are used to calculate axial and radial strains in the powder material from the assumed displacement field. The resistance force of the active battery material, P_{powder}, (without foil) is defined by:

$$P_{powder} = 2\pi \int_0^{r_1} \sigma(\varepsilon) r\, dr \tag{3}$$

After integration, one gets:

$$P_{powder} = \frac{2\pi A R \delta^3}{3H^2} \tag{4}$$

For the contribution of the system of metallic foil, a simple rigid-plastic solution of a clamped thin membrane is used [17].

$$P_{foil} = \frac{2}{3}\pi\sigma_0 h_f N\delta \tag{5}$$

where h_f is the average thickness of a foil, and N is the total number of aluminum and copper foils. Also, note that σ_0 is the average flow stress of aluminum and copper foils.

The total punch force P is calculated by adding the resistance of active powder material and foil, $P = P_{powder} + P_{foil}$. The above solutions were plotted for the following measured values of material and geometrical parameters presented in Table 3:

$$P = 0.3\delta^3 + 0.48\delta \quad \text{(kN)} \tag{6}$$

Table 3
Measured values and parameters of the cell.

A (N mm^{-1})	R (mm)	H (mm)	σ_0 (N mm^{-2})	h_f (mm)	N
566	6	4.8	200	0.025	46

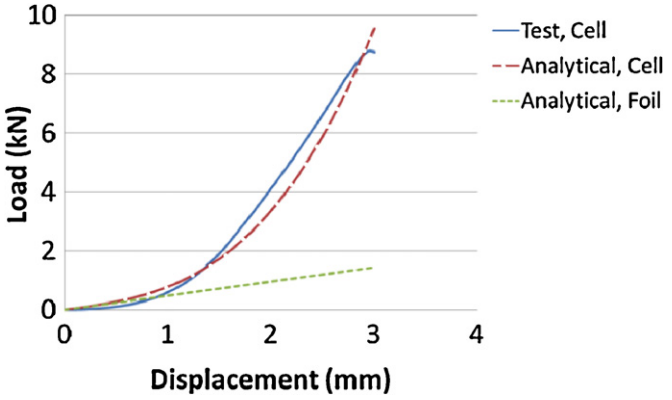

Fig. 8. Analytical vs experimental load–displacement curve for punch indentation of a bare cell.

A very good agreement was obtained between the analytical prediction and experimental load–displacement curve, as shown in Fig. 8. The closed-form solution identifies all geometrical parameters of the cell. The active material with binder is defined by the amplitude A of the quadratic power law. The strength of the separator is of the same magnitude as that of the powder and is therefore lumped in the constant A. The dotted straight line in Fig. 8 represents the contribution of foils alone. The above solution can be used for a preliminary design of batteries from the point of view of indentation by a foreign object. Combined with simple indentation test in a cell, they also could serve for a rapid determination of the uniaxial stress–strain curve of the coated material.

3.4. Unconfined axial crush of the cell in the width and length direction

Again, both bare and pouched cells were tested in the wide-column buckling configuration. Compression tests were performed in the width and length direction. These axial crush tests required the use of a retention device which prevented the cells from sliding to the side. Providing this was an aluminum plate with a rectangular groove machined to the thickness of the cell, which provided approximately pin–pin boundary conditions. In this type of test, dramatic differences in force levels were noticed for the bare versus pouched cells. In both cases there was an almost linear initial pre-buckling response. However, the bare batteries buckled at a very low force level of 40 N. The load on the pouched cell continued to increase to 160 N, which is four times larger. Some amount of delamination was observed between the two subcomponents of the cell, as shown in Fig. 9. After buckling, the load was kept constant for a short while and then dropped in accord with the post buckling theory of Euler columns.

The difference between the force level of the pouch and bare cells could be easily explained by a simple model of a two layered composite beam/column. The pouch is keeping the two sub-parts together and therefore a model of a monolithic column with thickness t is appropriate. By contrast, in the bare column, each sub-part of thickness $t/2$ buckles separately.

From the above simple calculations (in Fig. 10), the ratio between the buckling force of the pouched and bare cells is $P_p/P_b = 4$ which is exactly what found in the test. The results of the above test and analysis provide important clues to the successful design of the compression tolerant cells by choosing a suitable type of outside casing (such as plastic, aluminum, composite, and steel) as well as the way individual sub-parts are wrapped inside the cell. It is also evident that there is no universal type of battery construction and its strength and abuse tolerance would depend on the interior design of the winding/folding/stacking process.

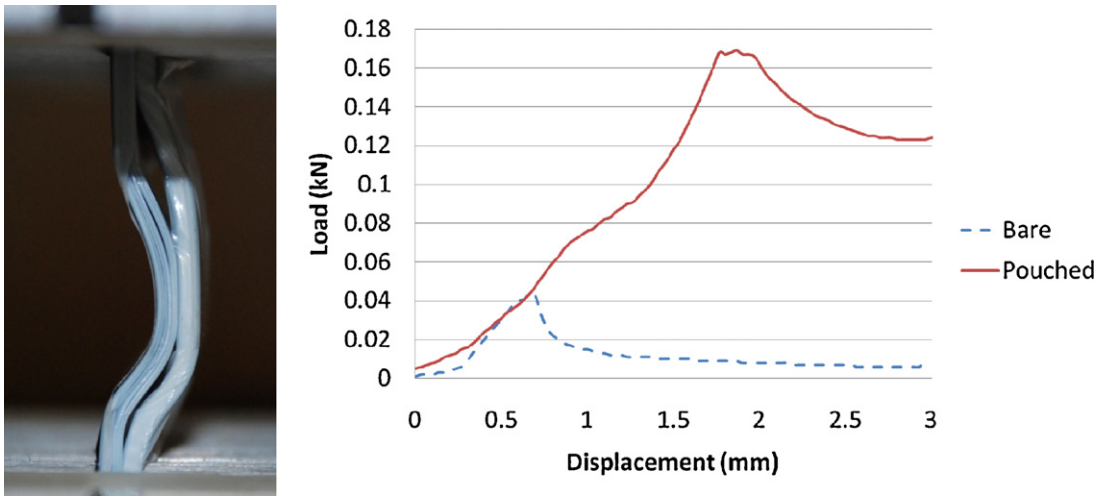

Fig. 9. Load–displacement response of bare and pouched cells compressed in the length direction.

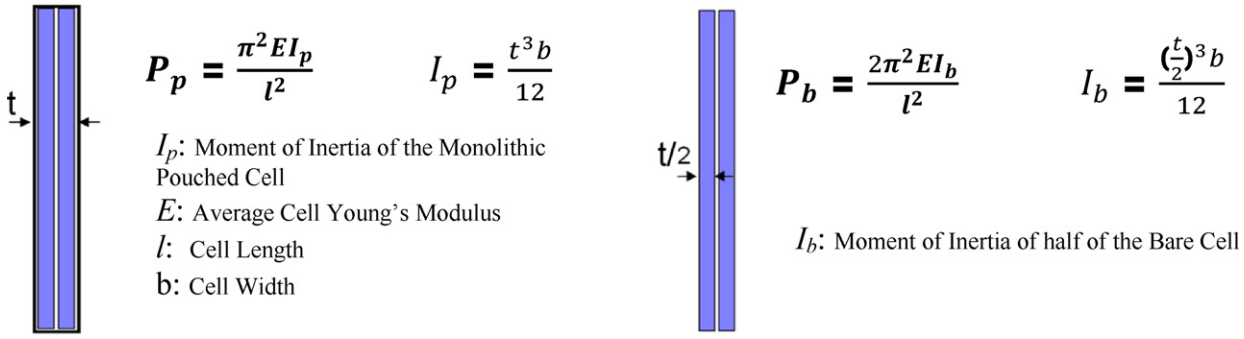

Fig. 10. Model of a monolithic pouched battery (left), and double layer bare battery (right).

3.5. *Confined compression test of the cell in the width direction*

Only bare cells were tested in a special fixture shown in Fig. 11. One confining plate was removed to show the interior of the crushed cell. Great care was taken in tightly fitting the fixture around the cell to minimize extrusion of cell material between adjoining faces of the fixture. The maximum travel of the punch was 13 mm. Electrolyte was observed to leak quite early in this test, indicating that the change in volume was partially due to escaping electrolyte from the porous media.

A considerable force of up to 60 kN was reached during this test. A photograph of the cross-section of the battery corresponding to the maximum punch travel is shown in Fig. 12 (left). At this stage, short wavelength buckles develop in an analogy of beam on foundation buckling [18]. The number of buckles along the length is 16. It would appear that the layers at the center of the battery have buckled first and subsequently brought the entire cross-section of battery into wave-like deformation. Similar deformation patterns were observed under compression of high-density honeycomb, Baker et al. [19].

The load–displacement data was converted into stress–strain curves and compared to the one generated from the lateral compression, Fig. 13. In both cases the state of strain was almost uni-axial and therefore, the comparison reveals the contribution

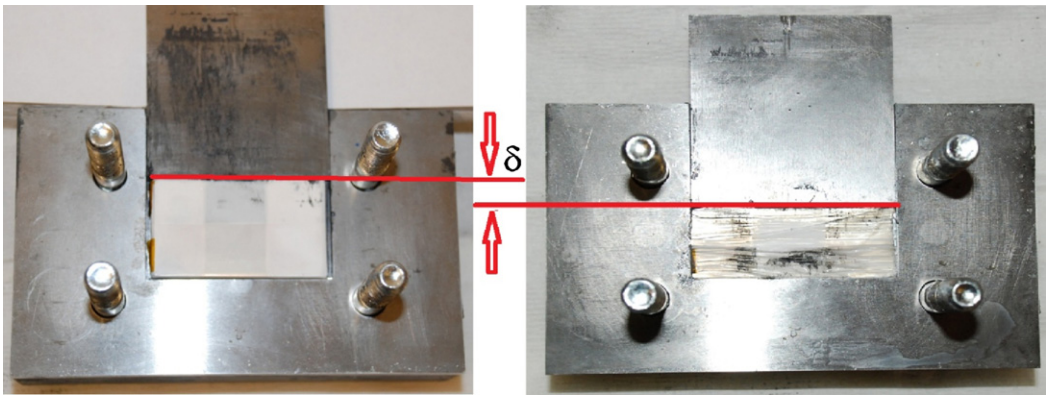

Fig. 11. Fixture with battery for confined compression test in the width direction, before and after test, with cover plate removed.

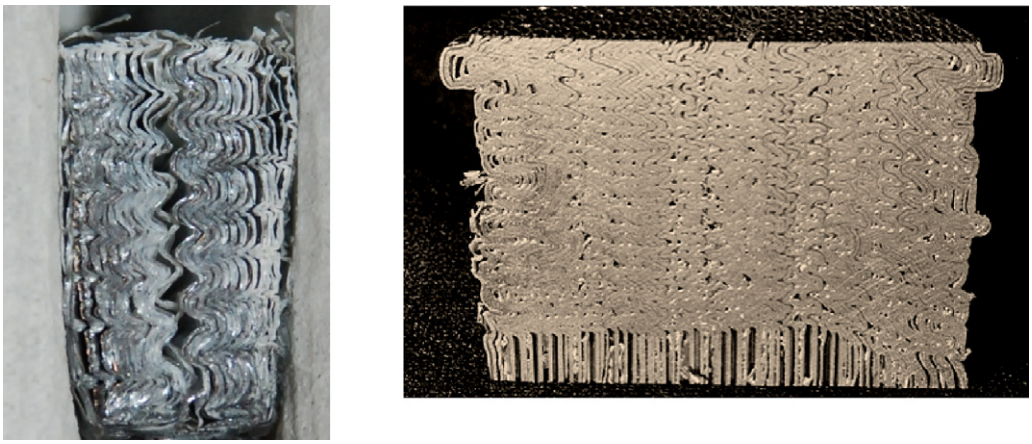

Fig. 12. Internal buckling and delamination in the axially compressed lithium-ion battery (left), and high density aluminum honey comb (right), Baker et al. [19].

of the aluminum and copper foil to the response of the system. In the lateral compression, the layers of the foil are normal to the loading direction and therefore do not contribute to the strength. In the present axial compression the layers of the foil are positioned along the direction of loading. The difference between the stress–strain curves obtained from lateral and axial compression is quite distinct in Fig. 13. The two curves diverge early on, at in-place displacement of less than 0.025 mm, and then stay parallel for the remainder of the process.

3.6. Analytical solution of the confined compression test

The compressive strain in this early stage is less than 0.001 so the aluminum and copper foils respond in the elastic range. The difference in the stress level can be explained and quantified using the solution for the beam on elastic foundation [18]. A simply supported Euler column buckles in the fundamental mode. The presence of foundation causes the column to buckle with higher modes. The textbook solution for the buckling load per unit width, N_w, is:

$$N_w = 2D\frac{n^2\pi^2}{l^2} \tag{7}$$

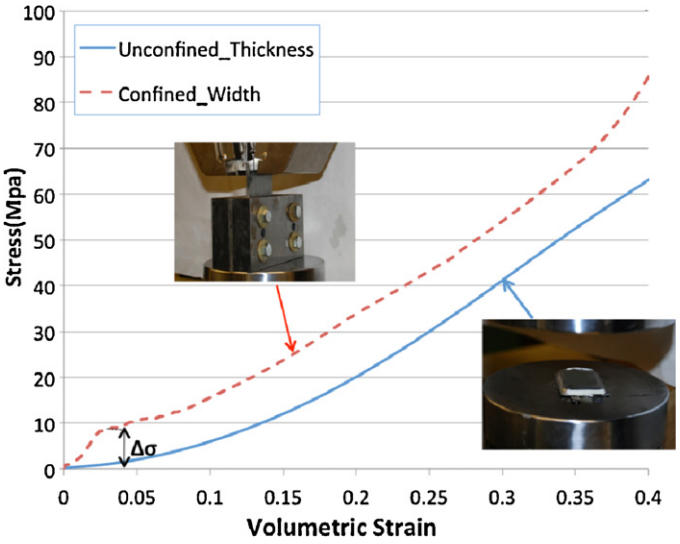

Fig. 13. Stress strain curve for confined compression in the width direction compared to unconfined compression.

where n is the number of half waves, D is the bending rigidity of the thin foil, $D = ((Et^3)/(12(1-\nu^2)))$, and t is the thickness of a single foil. Note, that the foundation constant in the above solution was replaced by the number of buckling half waves, n, which was measured. The buckling stress is obtained by dividing the total buckling load per unit width, P, by the corresponding thickness $\Delta\sigma_{foil} = P h^{-1}$, h being the thickness of the cell. Taking the measured values of $n = 16$, $E = 90$ GPa, l = 30 mm, $t = 0.025$ mm, the additional buckling strength offered by the system of foils is calculated to be $\Delta\sigma_{foil} = 9.03$ GPa. This value matches perfectly the difference in the two stress–strain curves presented in Fig. 13.

3.7. Three-point bending test of a medium-sized cell

A medium-sized cell of the length of 130 mm was chosen for this test as the larger size allowed the use of a 3-point loading fixture available at the lab, see Table 1. The radius of the roller support was 15 mm while the radius of the loading cylindrical punch was equal to the thickness of the cell which was 8 mm. The distance between supports was 95 mm with an overhang of 10.8 mm. As before, tests were conducted with and without the pouch covering. No local through-thickness indentation was observed. The tests of cells with and without pouch produced entirely different results (Figs. 14 and 15). The battery with pouch casing behaved as a regular simply supported beam undergoing three-point bending. A photograph sequence of this test is shown in Fig. 14. The fold developed in the shell casing on the compressive side leading to the shift of the neutral axis and the corresponding drop in the bending capacity of the center section. As a result a plastic hinge developed under the punch with a straight section of the beam on both sides. This behavior is well understood and predictable.

In the subsequent test the pouch casing was removed and the bare battery was placed in the same fixture. Here the deformation mode resembled that of a clamped beam even though it remained simply supported, Fig. 15.

In order to prevent sliding of the ends from the supports the punch travel was limited to 25 mm. The comparison of the load–displacement relation for the pouch and bare battery is shown in Fig. 16. This was the most unexpected and bizarre observation of the entire experimental program. The full explanation would require a very detailed analysis of the delamination process and interactions including the effects of the friction between layers of electrodes and separator, which is the subject of future upcoming research. However, one can provide a simple qualitative explanation of the experimental observation.

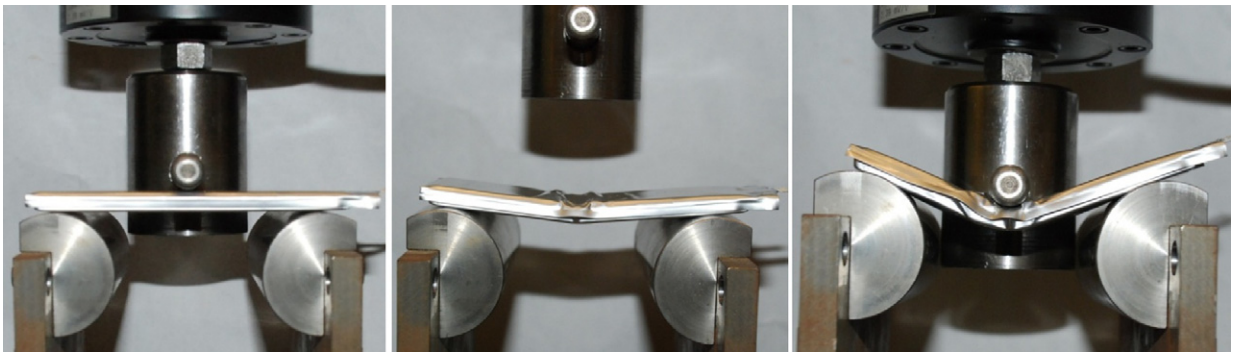

Fig. 14. Experimental setup and deformation sequence of a three-point bending of a battery with pouch.

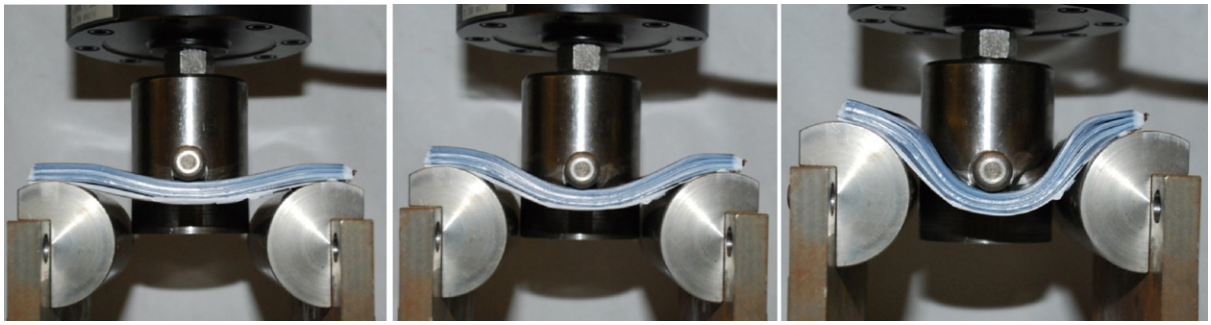

Fig. 15. Experimental setup and deformation sequence of a three-point bending of a bare battery without pouch.

The strength of the pouch battery is shown to be 5 times larger than that of the bare cell. These results underscore the vital importance of designing a proper shell-casing for any type of battery.

3.8. Analytical explanation of three-point bending

Tests on 3-point loading of pouched and bare batteries throw some light on the interactive process between individual layers of prismatic batteries. The cell wrapped in the pouch casing deflected initially as a pin–pin monolithic beam with a constant stiffness of K. From the bending solution with the point load in the center, the elastic stiffness is:

$$K = \frac{4Ebt^3}{l^3} \tag{8}$$

The above equation can be used to calculate the average elastic modulus of the battery from the measured stiffness, K. Interesting things are observed in the 3-point bending tests of the bare beam. In the 3-point bending, there is a linear variation of the bending moment along the beam with the maximum moment at the mid-span and zero at the support. And yet, the curvature of the beam is reversed resembling that of a fully clamped beam. What invisible reaction moment is causing zero slope at the support? One possible explanation is the presence of friction between apparently unconnected layers. With no friction, the laminated beam deforms as a bundle of n unconnected thin layers where the tension fibers of the top beam are in contact with the compressive fibers of the bottom layers. This gives rise to a length difference, Δu at the end points of each layer, Fig. 17.

$$\Delta u = \frac{tdw}{ndx} \tag{9}$$

where (dw/dx) is the slope of the deflected beam at the end point and t/n is the thickness of an individual layer. The moment of inertia

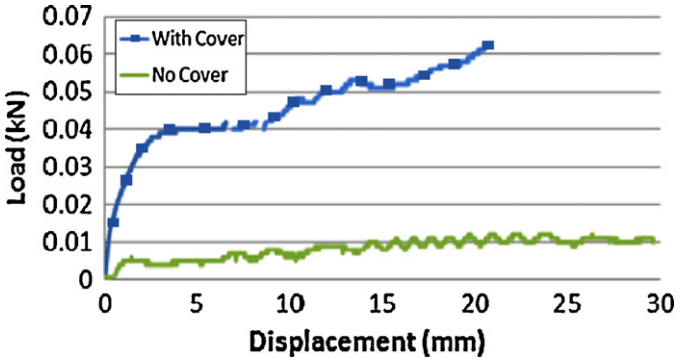

Fig. 16. Comparison of measured load–displacement curves of pouch and bare cells subject to 3-pt bending.

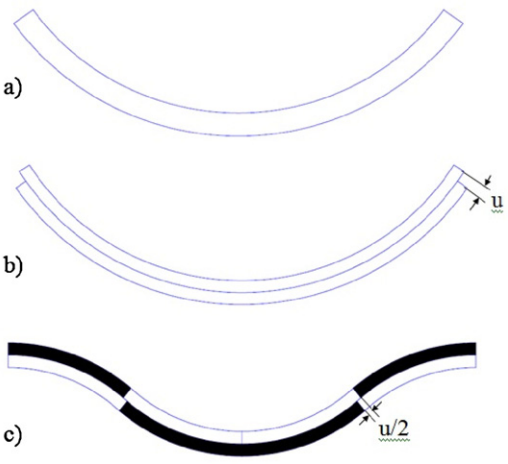

Fig. 17. Conceptual graphs showing the amount of interfacial slip in beam with monotonic and reverse curvature.

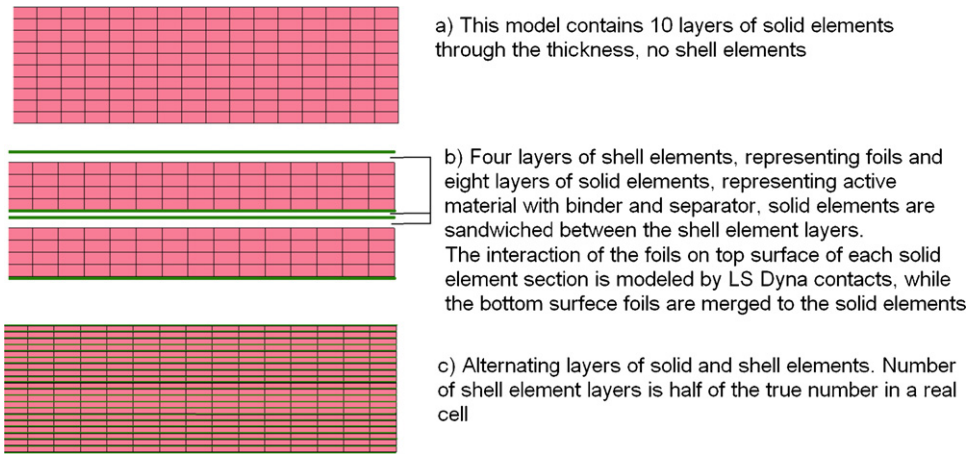

Fig. 18. Three FE element models used in the simulations.

of each layer is $b(t/n)^3(1/12)$ and there are n layers. Thus the stiffness of the composite beam, K_1, is diminishing with the sequence of number of layers.

$$K_1 = \frac{4Ebt^3}{l^3}\frac{1}{n^2} \tag{10}$$

For $n = 2$, there is a factor of four difference between the Eqs. (8) and (9). The factor of four is exactly the ratio of stiffness between the clamped beam (deflection shape c in Fig. 17) and simply supported beam (deflection shapes a and b in Fig. 17). A small additional work of friction $\mu P\Delta u$ between the layers of laminated structure is just sufficient to favor the beam to deflect in the "clamped" mode, case c, rather than the simply supported mode, case a or b.

This analysis underscores the importance and difficulties of correctly modeling the laminated prismatic cell with loosely connected layers.

4. Development of finite element model

LS Dyna version 971 nonlinear finite element software was used for modeling. The finite element model of the cell was constructed in three steps, for the through-thickness compression test, for the punch test, and for the confined compression test.

4.1. Lateral compression of battery

In the first step, the whole cell was modeled using fully integrated solid elements. The element size in both the length and width direction was 1 mm, and in thickness direction, 0.48 mm. Thus there were 10 elements through the thickness, Fig. 18a. A crushable foam material from the library of LS Dyna materials (Material 63) was used to model the homogenized behavior of the cell in through-thickness compression. It is believed that the behavior in this direction is mostly a function of the active material and binder properties rather than the aluminum/copper foils, therefore those structures were not modeled for this simulation. The average stress–volumetric strain properties presented in Fig. 19 are derived from the uni-axial compression experiments shown in Fig. 4. The modulus of elasticity (E) for tensile loading is considered as the maximum slope of the stress–volumetric strain curve as $E = 500$ MPa. Due to porosity of the cell, the material is believed to be highly compressive. The Poisson's ratio was assumed to be 0.01.

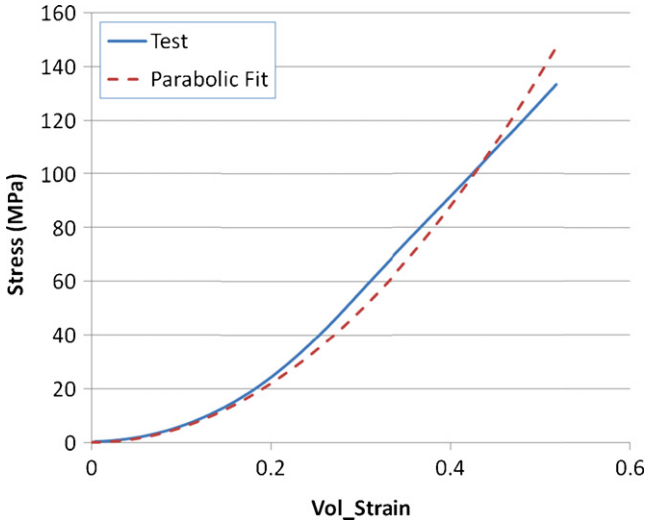

Fig. 19. Experimental stress-volumetric strain curve in through thickness unconfined compression.

A finite rigid wall was modeled under the solid elements. The rigid wall constrains the motion in the Z direction, also, the applied load to the cell is measured from the reaction force of the wall. On the top surface of the cell the contact-entity feature is used to model a rigid flat plate uniformly moving downward. This represents travel of the punch. The displacement was measured from the nodes on the top surface of the cell elements, which were in contact with this plate.

Fig. 20 shows the finite element model of the cell and the comparison of load–displacement curve for the model versus the tested cell. It can be observed that the crushable foam model can closely represent mechanical properties of the cell in uni-axial through-thickness compression tests.

4.2. Punch indentation simulation

In the next step of modeling, the punch indentation test was simulated. This simulation was done in two ways: first by using the same solid element model that was explained in the previous section, and second by introducing four layers of foil which represents the aluminum and copper foils present in the cell, Fig. 18c. The crushable foam material used for these simulations accepts a

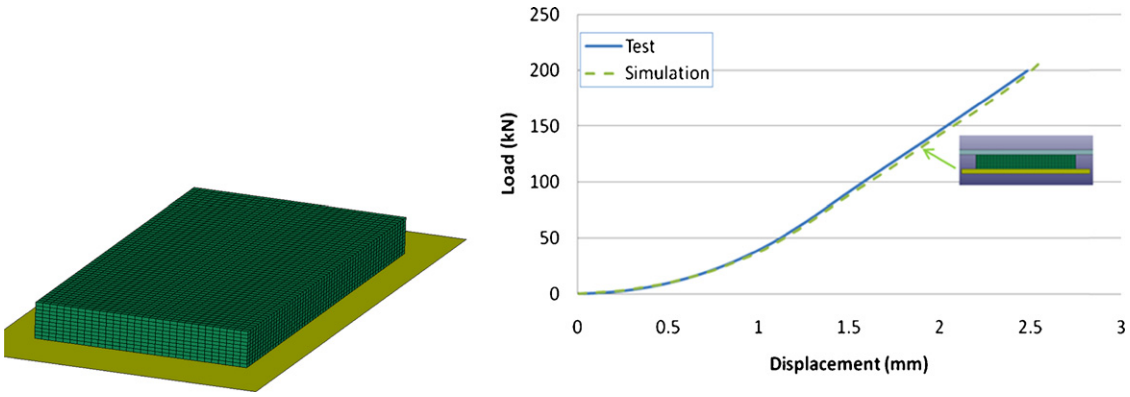

Fig. 20. Finite element model of the cell (left) and comparison of load displacement curve from simulation versus the test (right).

tensile cut-off value. This value is very important for realistic behavior of the cell under hemispherical punch indentation. The average tensile strength of the battery cell can be calculated from the yield strength of each of its components by using:

$$\sigma_{\text{tensile}} = \frac{\sum_{i=1}^{5} \sigma_i t_i n_i}{\sum_{i=1}^{5} t_i n_i} \tag{11}$$

where i represents the five layers of material in the battery cross section, σ_i is the yield strength of the component, t_i is the thickness of that layer, and n_i is the number of layers. Reports from literature on tensile strength of each layer were used to calculate the average tensile strength. Tensile strengths, σ_i, for aluminum and copper foils are listed in Shim et al. [20]. For the active anode and cathode particles, σ_i comes from the strength of the binder, and can be assumed to be the same. Liu et al. report on strength of cathodes in tension to be between 2 and 12 MPa, depending on the manufacturing process [11]. Dijan et al. report tensile strength of a Celgard separator to be 60 MPa [21]. Considering these values, the average tensile strength could be up to 55.58 MPa. This value was used for the simulations. Fig. 21 demonstrates the deformation of the cell (the model with only solid elements) after the first punch indentation simulation. This simulation is compared with the result of a pouched cell hemispherical punch test, where the pouch prevented delamination of the layers. Simulation also predicts point of failure of the material in tension, which is corespondent to the point of short-circuit from the partially charged battery test.

In a second model of punch indentation, four layers of shell elements were used to model properties of the foils. Two layers were on each side of the cell, and two layers in the middle. The thickness was considered as 0.26 mm. Shell elements were 1 mm × 1 mm in size. A piecewise linear-plasticity material model from library of LS Dyna materials was used to model properties of the aluminum/copper foils. The solid elements were given the same material properties of crushable foam that was explained in the previous section. A rigid sphere of 6.35 mm was used to model the hemispherical punch. Fig. 22 shows the second punch simulation (with foils). Comparison of force–displacement curve for this simulation against the hemispherical punch test without cover closely represented force–displacement behavior of the cell in the punch-indentation test, up to the end of simulation. Separation of the top foil layer represents delamination of the cell as observed through the hemispherical punch test.

The simulation predicts buckling of the faceplate in the width's direction. Clearly the material in the width direction is being drawn inside the created cavity and the in-plane radial motion produces considerable hoop stresses and leads to buckling. At the same time, the boundary in the length's direction is much further away. The material is not being drawn and instead the sheet under the punch is subjected to tensile load. The present simulation was able to capture this interesting effect. This builds an interesting implication on possible rupture of foil and separator under the punch.

4.3. Confined compression simulation

In the third part of simulations, the confined compression in the width direction was modeled. To model the buckling of layers as observed in the experimental test, it was required to represent the metal foil layers in a more realistic way. Therefore, metal foils were modeled with adding shell elements on the top and bottom surfaces of each layer of solid element, Fig. 18c. Considering solid elements of 0.24 mm in depth, it yields that each solid element represents one layer of the multi-material system which includes two foils. This model was used to show a qualitative representation of the

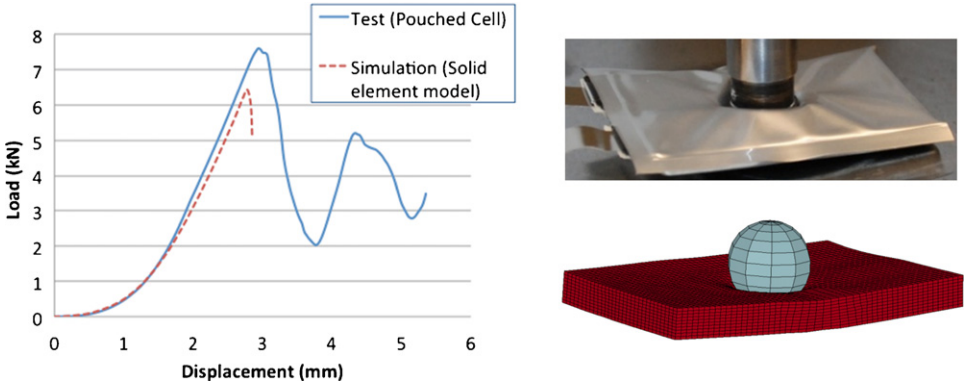

Fig. 21. Deformation and load–displacement history of the cell during punch indentation simulation.

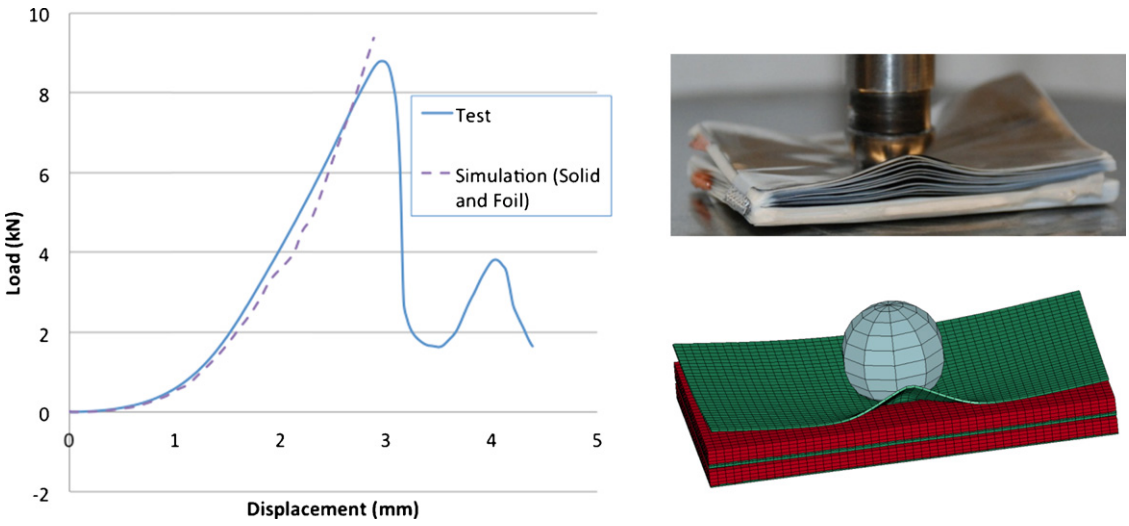

Fig. 22. Comparison of hemispherical punch test with the simulation.

buckling phenomena. However, as the number of foils is half of its real value, their cross sections are 0.03 mm to represent a similar order of moment of inertia. A more detailed model of layers will be built in the future to capture properties of the cell more realistically in this direction. Fig. 23 shows the formation of buckling waves in the layers of foil through the cross section. It can be observed that first waves were formed at the center of cross section and then consequent wave formation continued throughout the height of the cell. This type of wave formation indicates that foils underwent elastic buckling but due to confinement and the foundation of active powder material represented by solid elements, buckling mode is of a higher order rather than a single half-wave bending. Fig. 24 shows the load–displacement curve from simulation compared to the test. The curve was moved 0.6 mm forward, because the model had no imperfection, and onset of buckling was before progress of any displacement, while it is not the case in real tests.

The current model for the confined compression included 30,000 solid and 31,500 shell elements. Using 6 CPU's to run the simulation, it took 22 h to run. For a more representative model, it would be ideal to model all 42 layers of foil with their actual thickness. However, doing so would have required reducing the thickness of solid elements to 0.12 mm, and consequently would decrease the time step size. The time step could be controlled using mass scaling methods, as the current simulation is quasi-static, but if using this method, the model would not be useful for dynamic simulations in future. Another issue is that decreasing length of element in thickness direction to 0.12 mm would require

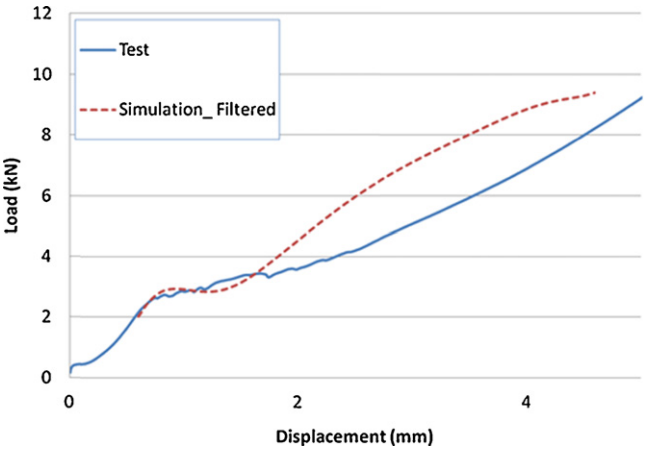

Fig. 24. Load displacement curve from confined compression test compared with the simulation.

decreasing the element size in length and width direction as well. It is recommended that the aspect ratio of elements remain under 5/1 which means the maximum element size in width and length direction would also decrease to 0.6 mm or smaller. This would cause an increase of about 8 times in the number of solid elements, and therefore, it would cause another significant increase in total

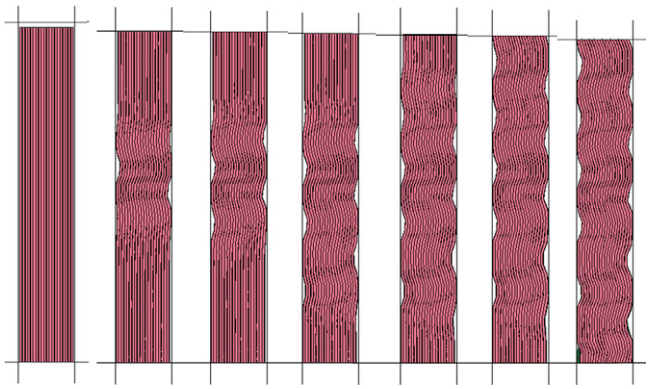

Fig. 23. Confined compression of the cell in width direction showing development of multiple buckles.

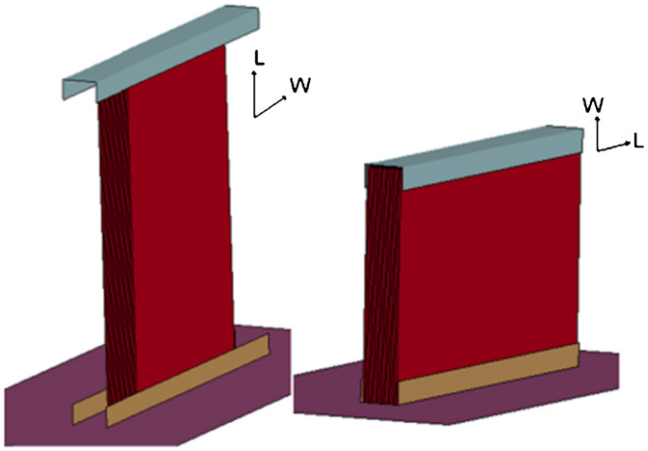

Fig. 25. The models of unconfined compression in width and length directions.

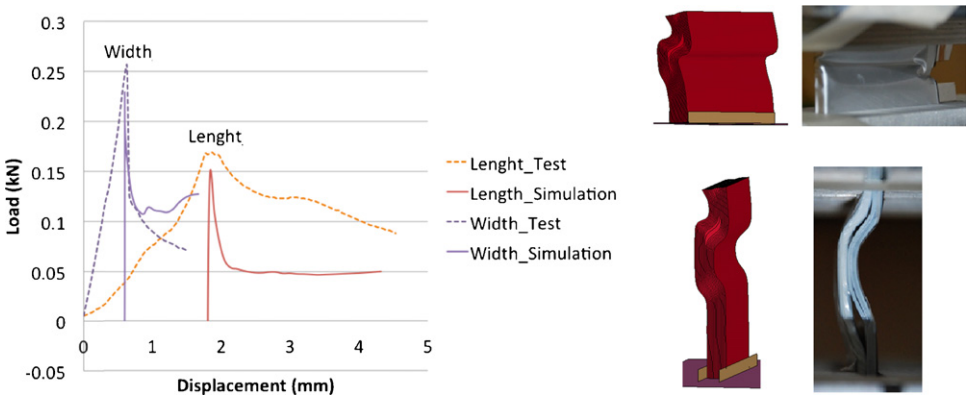

Fig. 26. Load displacement relationship (left) and geometry of the cells (right) from unconfined compression simulations.

CPU usage and simulation time. Therefore, a more refined mesh was not used for purpose of the current study.

4.4. Unconfined compression simulation

The same cell model that was developed for confined compression simulation, Fig. 18c, was used to model unconfined compression scenarios as well. The environment for the model was edited to include two fixtures to hold the cells on the top and bottom edges. The bottom fixture is fixed in its location, while the top fixtures applies the displacement to the cell. The unconfined compression was modeled in width and length directions, see Fig. 25.

Results show that the model was able to predict the shear buckling and delamination of the layers in both simulations see Fig. 26 (right). The load displacement curves show that the peak loads were also closely predicted. However, the model has a limitation in predicting pre-buckling load displacement curves as the model does not include any imperfections on the top contact surface.

5. Discussion

There has been a debate within the battery industry about the merits of using the cylindrical or prismatic batteries in vehicles from the point of view of mechanical integrity [22]. It is difficult to draw definite conclusions because of the multitude of factors that may affect performance of the cell. It transpires from the results of the present study and our research on cylindrical cells [12] that the structural integrity of the cylindrical battery is consistent and high in all loading directions. At the same time prismatic/pouch batteries are strong when compressed in the thickness direction and weak in other directions. The average mechanical properties of the RVE in the cylindrical cells are almost the same in all three directions leading to a quasi-isotropic material model. The comparison of the stress–strain curve of the cylindrical cell with that of the active material with binder in the prismatic cells is shown in Fig. 27. The shape of the two curves is entirely different. A full understanding of the above distinct behavior would entail a detailed analysis of buckling, delamination, and friction between the subsequent layers, which is the subject of the current work.

The cylindrical and prismatic cells compared in this study have the same $LiCoO_2$/graphite chemistry. Further information about porosity of the components was not available from manufacturers, due to proprietary nature of such information. It is believed that the most important source of the difference between these two cells could come from the form factor itself, meaning that there is different amount of constraint in the wound versus folded arrangement of the multi-layer system. It also should be mentioned that the stress–strain curve for the cylindrical batteries is a representative of the active material with binder and the separator combined with the foils. However, the stress–strain curve for the pouch batteries was extracted from the compression test that did not bring the role of foils into play. Note that shell elements were added to the solid elements to represent the entire battery as explained in Section 4. It can be concluded that there is no one universal stress strain curve that could be used for all types of batteries and that different testing procedures should be used depending on the form factor of the cell.

The present paper has identified the importance of the amount of lateral battery constraints on its strength. Only two limiting cases were considered; one with unconfined compression and the other with full confinement. For the development of constitutive models and to better understand the local deformation mechanisms, a test program should be designed with a controlled amount of pre-compression. A suitable device was constructed in the Impact and Crashworthiness Lab at MIT, Fig. 28, and will be used to extend the validity of the present model.

The dense mesh shown in Fig. 18c brings a total number of FE to 61,500 for a relatively small size 30 mm × 50 mm cell. Cells used for EV are much larger of the order of 250 mm × 250 mm. Keeping this level of resolution in modeling real electric vehicle such as GM Volt will end up with 2.5 million elements for a single pouch cell. There are 288 such cells in the GM Volt battery pack, which will bring the total number of FE elements unmanageable. It looks that the present limit of computational power restricts the level of cell discretization and element size. The intermediate mesh, Fig. 18b

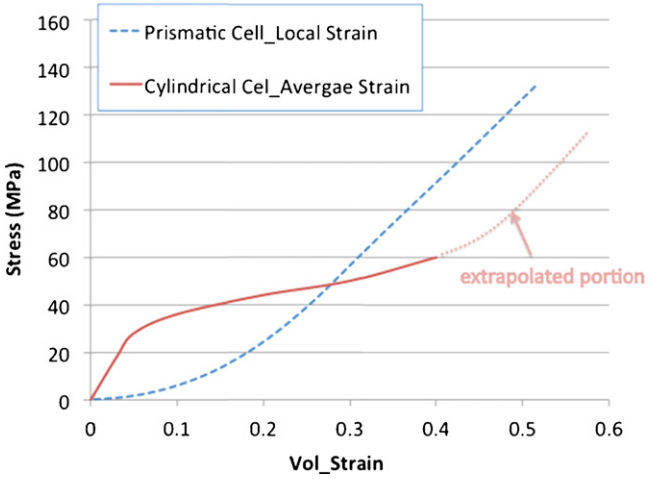

Fig. 27. Comparison of the average stress–volumetric strain of the cylindrical battery (combined effect of all layers) and the local stress–strain curve of the rectilinear battery (foil not included).

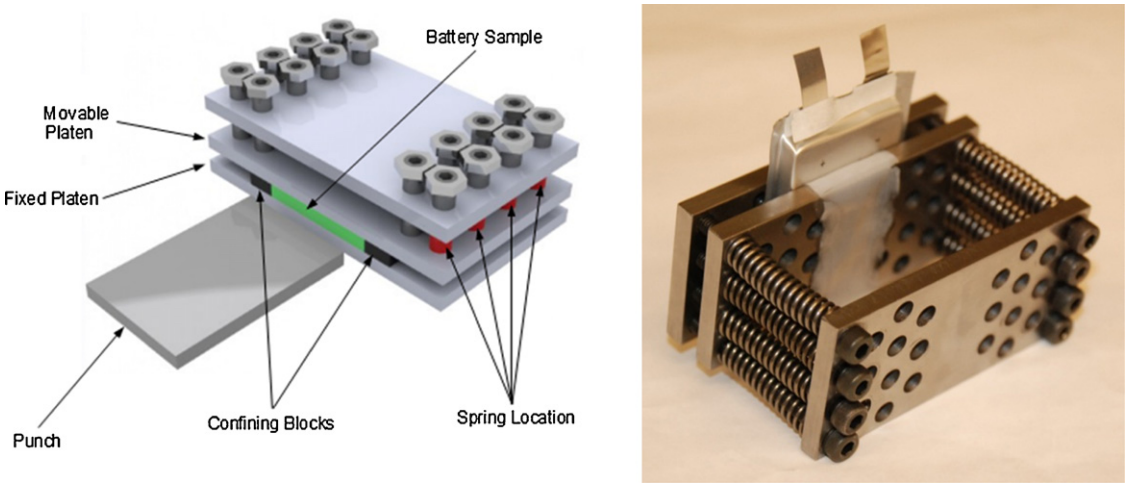

Fig. 28. Prototype of the plane–strain compression of pouched batteries with an adjustable confinement.

brings the total number of elements for one cell to 7500. Such a mesh will not be able to describe local short buckling waves in fully confined compression, but would most probably adequate to describe all other loading cases. Yet, this level of discretization would still results in 2.1 million elements for the entire battery pack. It is clear that for efficient FE modeling of a vehicle car body, one would have to sacrifice the accuracy by using still larger element size through the thickness of the cell.

6. Conclusions

The main objective of the present research was to extract and document mechanical properties of a prismatic/pouch cell valid in various mechanical abuse scenarios leading to large deformation and possible short circuit. The strain stress properties of the cell in different loading situations were obtained from a comprehensive set of 17 tests. Then analytical solutions were used to interpret the relative contribution of various layers to the overall strength of the battery cell, which helped to construct a simple numerical model. The generated experimental data were sufficient to generate the first level constitutive model of the battery cell and perform FE simulations. Accurate prediction was obtained for the level of forces and deformation mode of cells in all of the loading scenarios simulated. The present homogenized material model could be used to advance the understanding of the battery response in two different levels. First, it provides the far field state of stress and strain in the cell, which is needed in a multi-scale approach to predict possible short circuit due to a local failure at the level of electrode/separator assembly. Going in the different direction across the length scale, the computational model of an individual cell provides the fundamental building block for battery modules and battery packs.

From the present experimental and computational study the following specific conclusions may be drawn:

(i) A finite element model of a small pouch battery was developed capable of predicting load and displacement due to external object intrusion. The model also predicts onset of short circuit during a punch loading with very good accuracy.
(ii) A suitably calibrated crushable foam material is shown to be accurate to simulate the response of the pouch batteries in three loading configurations: through thickness compression, local punch indentation, and axial compression (confined and unconfined).
(iii) Pouched and bare batteries (without the cover) exhibited different failure modes and produce different force levels in bending and unconfined buckling tests. In the case of the present batteries, the shell casings were made of thin, approximately 0.1 mm foil. It was interesting to see that such an apparently thin membrane with very low bending stiffness could exert significant confinement to the cell and thus change its properties. This observation indicates the importance of a properly designed shell casing for any type of prismatic battery. For the wound cylindrical batteries, each subsequent layer provides confinement to interior layers, therefore, the thickness of the shell casing may not be that important.
(iv) The test and simulation proved that the layered structure of flat prismatic batteries is structurally anisotropic where the strengths in the in-plane direction depends on the amount of lateral confinement, and in general is different from the strengths in through thickness direction. The structural anisotropy comes from the layered nature of the battery interior were no tension and limited shear is transferred at the interface of various layers.
(v) The theoretical analysis and numerical simulation of the confined compression prove that there is an intrinsic scaled parameter characterizing the lengths of the internal buckling waves in fully confined test. The challenge is to include this parameter in a complete constitutive model of the battery interior.
(vi) Finally, it is clear that there is no universal constitutive model to represent all types of batteries with different types of external casing and shape factor.

The ongoing research for the Battery Consortium at the Impact and Crashworthiness Lab at MIT will gradually resolve a number of outstanding issues identified in the present paper.

Acknowledgements

Part of this work is supported through the International Battery Consortium at MIT. Thanks are due to John Campbell for performing additional set of experiments with voltage measurement.

References

[1] R. Deshpande, Y.T. Cheng, M.W. Verbrugge, J. Power Sources 195 (2010) 5081–5088.
[2] S. Golmon, K. Maute, M.L. Dunn, Comput. Struct. 87 (2009) 1567–1579.
[3] H. Hu, X. Zhao, Z. Suo, J. Mater. Res. 25 (2010) 1007–1010.
[4] X. Xiao, W. Wu, X. Huang, J. Power Sources 195 (2010) 7649–7660.
[5] X. Zhang, A.M. Sastry, W. Shyy, J. Electrochem. Soc. 155 (2008) A542.
[6] X. Zhang, W. Shyy, A.M. Sastry, J. Electrochem. Soc. 154 (2007) A910.

[7] R. Deshpande, Y. Qi, Y.T. Cheng, J. Electrochem. Soc. 157 (2010) A967.
[8] K. Zhao, W.L. Wang, J. Gregoire, M. Pharr, Z. Suo, J. Vlassak, E. Kaxiras, Nano Lett. 11 (2011) 2962–2967.
[9] L.Q. Zhang, X. Liu, Y. Liu, S. Huang, T. Zhu, L. Gui, C. Wang, S. Mao, Z. Ye, J.P. Sullivan, ACS Nano 5 (2011) 4800–4809.
[10] W. Cai, H. Wang, H. Maleki, J. Howard, E. Lara-Cursio, J. Power Sources 196 (2011) 7779–7783.
[11] P. Liu, E. Sherman, A. Jacobsen, J. Power Sources 189 (2009) 646–650.
[12] E. Sahraei, R. Hill, T. Wierzbicki, Proc. of the Battery Congress, Ann Arbor, MI, 2011.
[13] I. Rohr, J. Campbell, E. Sahraei, T. Wierzbicki, CrashMAT Conference, unpublished results, 2011.
[14] C. Ashtiani, AABC-09 Conference, 2009.
[15] J. Nguyen, C. Taylor, INTELEC 2004, IEEE, 2004, pp. 146–148.
[16] M. Otsuki, T. Ogino, K. Amine, ECS Trans. 1 (2006) 13–19.
[17] Tomasz Wierzbicki, 2.081J/16.230J, 2008.
[18] S. Timoshenko, Theory of Elastic Stability, New York, McGraw-Hill, 1936.
[19] W. Baker, T. Togami, J. Weydert, Int. J. Impact Eng. 21 (1998) 149–163.
[20] K. Shim, S. Lee, B. Kang, S. Hwang, J. Mater. Process. Technol. 155 (2004) 1935–1942.
[21] D. Djian, F. Alloin, S. Martinet, H. Lignier, J. Power Sources 187 (2009) 575–580.
[22] Berchevskiy, personal communication, 2010.